Dimensional Diversity in Transition Metal Trihalides

Jianhua Lin and Gordon J. Miller*

Department of Chemistry, Iowa State University, Ames, Iowa 50011

Received November 6, 1992

Structural variations of the second- and third-row transition metal trihalides are rationalized via tight-binding band calculations and evaluation of Madelung energetic factors. The observed structure for a given metal halide is controlled by both the coordination geometry at the anion and the d electron configuration at the metal. As the polarizability of the halide increases, the M-X-M angle, in general, decreases so that three-dimensional frameworks occur for the fluorides, while layer and chain structures are found for the chlorides, bromides, and iodides. Within a particular halide system, systematic structural trends also occur as the d electron configuration changes.

Few classes of inorganic solids can surpass the diverse chemical and physical attributes of the transition metal halides.[1,2] Through literally countless studies in the literature, each transition element provides a fascinating individual collection of structures and properties, although, as chemists, we are always trying to ascertain periodic trends and relationships from one metal to the next. From a theoretical perspective, these compounds have provided a basis for testing various crystal field and ligand field theories due to the large electronegativity and size of the halide anions with respect to the transition metal cations.[3,4] The increased size factor of the second- and third-row metals provides additional forces that compete with the omnipresent attractive cation-anion and repulsive anion-anion interactions.

Most transition metal trihalides have structures based upon close packings of halides with the metal ions in octahedral holes.[5] Exceptions include the ones with the larger lanthanide elements (La to Gd), in which the cation coordination number is 9, those of W and Re with the metal atoms in a five-coordinate square pyramidal anionic environment,[6] and the series AuX_3 with square planar coordinated Au atoms.[7] Nevertheless, the stoichiometric ratio in the transition metal trihalides provides structures that can range from one- to three-dimensional arrangements. What factors govern the dimensionality of a given compound, and how does it affect physical properties?

In this contribution we present a detailed analysis of the electronic structure and chemical bonding in the trihalides of the second- and third-row transition metals. We shall probe the effect of valence electron concentration on structural preference, as well as evaluate how the preferred local coordination geometries at the halide ion influence the choice of a complete structure.

Review of Structural Details

Most transition metal trihalides with six-coordinate metal and two-coordinate halogen atoms adopt one of the following structure types (or some distorted variant): VF_3, BiI_3, $AlCl_3$, or TiI_3, all of which are based upon a nearly close packing of anions with the metal atoms in one-third of the octahedral interstices.[5] The major differences occur in either the three-dimensional anion packing modes or the distribution of occupied metal sites.

All known trifluorides are related to the VF_3 structure, which represents an intermediate geometry between the cubic ReO_3-type and the rhombohedral RhF_3-type.[8] RhF_3 contains a hexagonally close packed (hcp) arrangement of fluoride ions. As Michel et al. have shown, these materials consist of an array of chains of rigid octahedra that have been rotated around their trigonal axes.[9,10] The MF_6 octahedral units remain virtually regular throughout the series, while the M-F-M angle varies from 180° in NbF_3 to 132° at RhF_3. Figure 1 illustrates the geometrical relationships between the three varieties of VF_3 structures. PdF_3, which was originally assigned the space group $R\bar{3}c$ (isostructural to RhF_3), in fact adopts a lower symmetry group ($R\bar{3}$) with two differently sized $[PdF_6]$ octahedra.[11] The compound is thus formulated as $Pd^{2+}Pd^{4+}F_6$, in which the Pd^{2+} coordination environment remains (unusually) octahedral.

While the trifluorides occur as three-dimensional networks, the heavier trihalides crystallize as either layer or chain structures.[7] The commonly observed layer structures are BiI_3 and $AlCl_3$, which correspond to ordered defect derivatives of the CdI_2 and $CdCl_2$ types, respectively.[7,12] Both consist of $^{\infty}_{2}[(\square X_{6/3})(MX_{6/3})_2]$ sheets ($\triangleq M_2X_6$; see Figure 2a), in which the metal atoms form a honeycomb network. The complete structures of BiI_3 and $AlCl_3$ form by stacking this two-dimensional motif in different ways: for rhombohedral BiI_3, the halide ions are hcp and, moreover, the vacancies in the metal layers spiral trigonally along the *c* direction; in the monoclinic $AlCl_3$ structure, the anions are cubic close packed (ccp), and the metal vacancies are ordered along the monoclinic *a* axis. In each case, the planes of possible metal atom sites alternate 66% and 0% occupancy along the stacking direction.

The structure of TiI_3, unlike $AlCl_3$ and BiI_3, is quasi-one-dimensional.[5,13,14] The anions in TiI_3 form a hcp arrangement, but the metal atoms occupy one-third of each plane to form quasi-infinite one-dimensional chains, $^{\infty}_{1}[MX_{6/3}]$, of face-sharing MX_6 octahedra. A projection of TiI_3 along the hexagonal *c* axis (Figure

(1) Greenwood, N. N.; Earnshaw, A. *Chemistry of the Elements*; Pergamon Press: Oxford, England, 1984.
(2) (a) Brown, D. *Halides of the Lanthanides and Actinides*; Wiley: New York, 1968. (b) Colton, R.; Canterford, J. H. *Halides of the First Row Transition Metals*; Wiley: New York, 1968. (c) Canterford, J. H.; Colton, R. *Halides of the Second and Third Row Transition Metals*; Wiley: New York, 1969.
(3) Ballhausen, C. J. *Introduction to Ligand Field Theory*; McGraw-Hill: New York, 1962.
(4) Dunn, T. M.; McClure, D. S.; Pearson, R. G. *Some Aspects of Crystal Field Theory*; Harper and Row: New York, 1965.
(5) Wells, A. F. *Structural Inorganic Chemistry*, 5th ed.; Oxford University Press: Oxford, England, 1984.
(6) Kepert, D. L. *The Early Transition Metals*; Academic Press: London, 1972.
(7) Hulliger, F. *Structural Chemistry of Layer-Type Phases*; D. Reidel Publishing Co.: Dordrecht, The Netherlands, 1976; p 164.
(8) Babel, D.; Tressaud, A. In *Inorganic Solid Fluorides*; Hagenmuller, P., Ed.; Academic Press: New York, 1985; p 77.
(9) Michel, C.; Moreau, J. M.; James, W. J. *Acta Crystallogr., Sect. B* **1971**, *B27*, 501.
(10) Hepworth, M. A.; Jack, K. H.; Peacock, R. D.; Westland, G. J. *Acta Crystallogr.* **1957**, *10*, 63.
(11) Tressaud, A.; Wintenberger, M.; Bartlett, N.; Hagenmuller, P. *C. R. Hebd. Seances Acad. Sci.* **1976**, *282*, 1069.
(12) Pearson, W. B. *The Crystal Chemistry and Physics of Metals and Alloys*; Wiley Interscience: New York, 1972.
(13) Natta, G.; Corrandini, P.; Bassi, I. E.; Porri, L. *Atti. Accad. Naz. Lincei, Cl. Sci. Fis., Mat. Nat., Rend.* **1958**, *24*, 121.
(14) Adams, D. M. *Inorganic Solids*; Wiley: London, 1974.

0020-1669/93/1332-1476$04.00/0

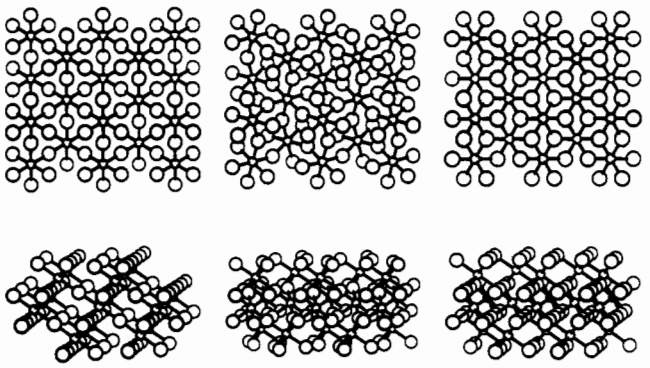

Figure 1. (001) (top) and (1$\bar{1}$0) (bottom) Projections of (a) NbF_3 (ReO_3-type), (b) MoF_3, RuF_3 (VF_3-type), and (c) RhF_3. Large open circles are F atoms; small open circles are metal atoms. The thickness of the open circles correlates with distance above the projection plane.

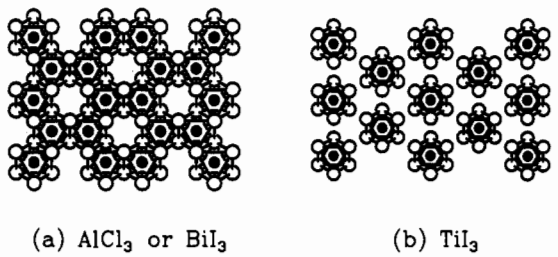

Figure 2. (a) Characteristic $^{\infty}_{2}[M_{2/3}X_2]$ layer in the $AlCl_3$ and BiI_3 structures. (b) Analogous projection of the regular TiI_3 structure. Large open circles are halide atoms; small dark circles are metal atoms.

Table I. Structures of the Second- and Third-Row Transition Metal Trihalides[7]

	metal	MF_3	MCl_3	MBr_3	MI_3
d^0	Y	YF_3	$AlCl_3$	BiI_3	BiI_3
	Lu	YF_3	$AlCl_3$	BiI_3	BiI_3
d^1	Zr		TiI_3	TiI_3	TiI_3
	Hf				TiI_3
d^2	Nb	ReO_3[a]	α-$Nb_{3-x}Cl_8$	α-$Nb_{3-x}Cl_8$	α-$Nb_{3-x}Cl_8$ β: TiI_3
	Ta	ReO_3[a]	α-$Nb_{3-x}Cl_8$	α-$Nb_{3-x}Cl_8$	
d^3	Mo	VF_3	α: $AlCl_3$ β: $MoCl_3$	TiI_3	TiI_3
	W		$[W_6Cl_{12}]Cl_6$	$[W_6Cl_{12}]Cl_6$	
d^4	Tc				
	Re		Re_3Cl_9	Re_3I_9	Re_3I_9
d^5	Ru	VF_3	α: $AlCl_3$ β: TiI_3	TiI_3	TiI_3
	Os		$AlCl_3$		TiI_3
d^6	Rh	RhF_3	α: $AlCl_3$ β: polytype	$AlCl_3$	$AlCl_3$
	Ir	RhF_3	α: $AlCl_3$ β: ortho. $IrCl_3$	$AlCl_3$	$AlCl_3$
d^7	Pd	PdF_3			
	Pt		$PtBr_3$	$PtBr_3$	
d^8	Au	AuF_3	Au_2Cl_6	Au_2Br_6	Au_2I_6
d^{10}	In	VF_3	$AlCl_3$	$AlCl_3$ BiI_3	$AlCl_3$ In_2I_6

[a] These phases are stabilized by small amounts of oxide ions.

2b) offers a comparative view to the distribution of occupied metal sites in the layered materials.

In addition to the vertical trends exhibited by the transition metal trihalides, they also vary systematically with d-count. These observations are summarized in Table I, in which the compounds are grouped according to the halide matrix. We begin our summary with the trifluorides.[5,7,8] The d^0 compounds generally do not adopt structures based upon octahedral coordination of the metal, and will not be considered in our discussion. No d^1 (except TiF_3) or d^4 systems have been noted. For d^2 and d^3 compounds, older literature reports the cubic ReO_3-type with the M–F–M angle of 180°; these were in fact oxyfluorides, $MO_{3x}F_{3-3x}$.[15] The highest purity of NbF_3 has been obtained by high-pressure synthesis,[16] and it retains the cubic structure. A careful neutron diffraction investigation on MoF_3 shows the VF_3-type and antiferromagnetic ordering of three unpaired spins per Mo atom.[17] In the d^5 and d^6 systems, the M–F–M bends significantly away from linearity to give the hcp-based RhF_3 structure type. We have already referred to the interesting case of PdF_3, which, in addition, shows ferromagnetic ordering with a T_C of 10 K.[18]

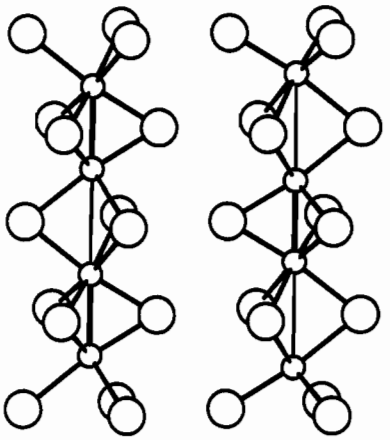

Figure 3. View along [100] in TiI_3 to illustrate the alternating metal–metal distances along the face-sharing octahedral chains.

The heavier trihalides show their own intrinsic structural systematics. Group 3 (d^0) compounds all adopt either the normal BiI_3 or $AlCl_3$ structure.[7] For the group 4 (d^1) metals, distorted TiI_3 structures are found.[19-21] The metal atoms in these compounds move away from their regular octahedral sites to form one-dimensional chains with alternating short and long metal–metal distances, as displayed in Figure 3 for ZrI_3. In group 5 (d^2) NbI_3 is the only reported compound. A recent X-ray diffraction study indicates that it also adopts the distorted TiI_3 structure with an extremely short Nb–Nb bond distance of 2.77 Å.[21] All of the other trihalides of this transition metal group, i.e., Nb and Ta, are not thermodynamically stable phases, but rather homogeneous mixtures of M_3X_8 and MX_4.[22]

The group 6 trihalides form three different kinds of structures. α-$MoCl_3$ crystallizes in a distorted $AlCl_3$ structure with Mo–Mo dimers.[23] β-$MoCl_3$, which also contains Mo–Mo pairs, is related to the BiI_3 phase.[23] Figure 4 illustrates the distortion of the metal arrangement in β-$MoCl_3$ from a regular honeycomb (6^3) net. The heavier halides, $MoBr_3$ and MoI_3, however, crystallize in the distorted TiI_3 structure with pairing of Mo atoms along the c axis.[21,24] WCl_3 and WBr_3 are exceptional cases which also show metal–metal bonding.[25,26] Although performed on powder samples, the structural analysis revealed W_6X_{18} ($\triangleq[W_6X_{12}X_6]$) clusters. Metal clusters continue into the group 7 (d^4) compounds as well. Although nothing is yet reported for the Tc system, all

(15) Chamberland, B. L. In *Inorganic Solid Fluorides*; Hagenmuller, P., Ed.; Academic Press: New York, 1985; p 205.
(16) Pouchard, M.; Torki, M. R.; Demazeau, G.; Hagenmuller, P. *C. R. Hebd. Seances Acad. Sci.* **1971**, *273*, 1093.
(17) Wilkinson, M. K.; Wollan, E. O.; Child, H. R.; Cable, J. W. *Phys. Rev.* **1961**, *121*, 74.
(18) Dance, J.-M.; Tressaud, A. In *Inorganic Solid Fluorides*; Hagenmuller, P., Ed.; Academic Press: New York, 1985; p 379.
(19) Lachgar, A.; Dudis, D. S.; Corbett, J. D. *Inorg. Chem.* **1990**, *29*, 2242.
(20) Lachgar, A.; Dudis, D. S.; Dorhout, P. K.; Corbett, J. D. *Inorg. Chem.* **1991**, *30*, 3321.
(21) Dorhout, P. K.; Corbett, J. D. *Inorg. Chem.* **1991**, *30*, 3326.
(22) Simon, A.; von Schnering, H. G. *J. Less-Common Met.* **1966**, *11*, 31.
(23) Schäfer, H.; von Schnering, H. G.; Tillack, J.; Kuhnen, F.; Wöhrle, H.; Bauman, H. *Z. Anorg. Allg. Chem.* **1967**, *353*, 281.
(24) Babel, D. *J. Solid State Chem.* **1972**, *4*, 410.
(25) Siepmann, R.; von Schnering, H. G.; Schäfer, H. *Angew. Chem.* **1967**, *79*, 650; *Angew. Chem., Int. Ed. Engl.* **1967**, *6*, 637.
(26) (a) Siepmann, R.; von Schnering, H. G. *Z. Anorg. Allg. Chem.* **1968**, *357*, 289. (b) Lange, U.; Schäfer, H. *J. Less-Common Met.* **1971**, *21*, 472.

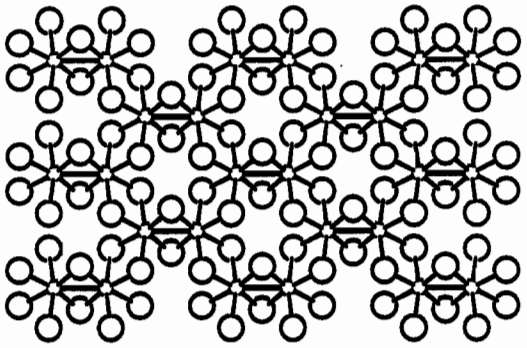

Figure 4. View along [001] in β-$MoCl_3$ to emphasize the distortion of the honeycomb network of metal atoms toward Mo–Mo dimers.

of the rhenium trihalides contain triangular rhenium clusters, Re_3X_9, which connect to three other neighboring clusters through bridging halogen atoms to form a buckled two-dimensional layer.[27,28] The coordination of Re atoms by the halide is a slightly distorted square pyramid. The group 8 (d^5) metal trihalides, in some cases, are very similar to that of d^1 systems. Distorted face-sharing octahedral chains $^{\infty}_{1}[MX_{6/2}]$ have been found for all ruthenium trihalides.[29,30] In addition, another modification of ruthenium trichloride, α-$RuCl_3$, is believed to belong to the $AlCl_3$ type by an X-ray powder diffraction study.[29] A recent structural investigation on α-$RuCl_3$ by means of scanning tunneling microscopy showed distortions of $[RuCl_6]$ octahedra on the surface of the crystal.[31] The images have been interpreted as a shift in surface chloride positions due to formation of Ru–Ru pairs. Although the structural arrangement in the crystalline bulk is still not clear, the distortion found on the surface of the crystal may indicate a similar distortion within the crystal. For the group 9 metals (d^6), we again find the regular $AlCl_3$ structure for all of the trihalides,[7,32] with numerous examples of stacking disorder. Pd does not form stable trihalides beyond the fluoride, but both $PtCl_3$ and $PtBr_3$ have been reported.[33,34] As in PdF_3, these compounds apparently contain Pt in two different oxidation states: 50% as Pt^{2+} in a $[Pt_6X_{12}]$ octahedral cluster and 50% as Pt^{4+} in $^{\infty}_{1}[PtX_2X_{4/2}]$ cis edge-sharing octahedral chains. Finally, Au forms stable molecular trihalides with each of the halides—Au_2X_6, with square-planar coordinated Au atoms.[7]

Computational Methods

In the following sections, we investigate the covalent and ionic forces responsible for the stability of one structural modification over another in the MX_3 family of compounds. Ionic energy terms are represented solely as the Madelung part of the total lattice energy and were evaluated using the Ewald method.[35] Our determination of the electronic structure utilized the tight-binding approximation (LCAO approximation) with the extended Hückel ansatz.[36] More details of our calculations are described in the Appendix.

(27) (a) Cotton, F. A.; Mague, J. T. *Proc. Chem. Soc.* **1964**, 233; *Inorg. Chem.* **1964**, *3*, 1402. (b) Bennett, M. J.; Cotton, F. A.; Foxman, B. M. *Inorg. Chem.* **1968**, *7*, 1563.
(28) Gelinek, J.; Rüdorff, W. *Naturwissenschaften* **1964**, *51*, 85.
(29) Fletcher, J. M.; Gardner, W. E.; Fox, A. C.; Topping, G. *J. Chem. Soc. A* **1967**, 1038.
(30) Brodersen, K.; Breitbach, H.-K.; Thiele, G. *Z. Anorg. Allg. Chem.* **1968**, *357*, 162.
(31) Cantow, H.-J.; Hillebrecht, H.; Magonov, S. N.; Rolter, H. W.; Drechsler, M.; Thiele, G. *Angew. Chem.* **1990**, *102*, 551; *Angew. Chem., Int. Ed. Engl.* **1990**, *29*, 537.
(32) Babel, D.; Deigner, P. *Z. Anorg. Allg. Chem.* **1965**, *339*, 57.
(33) Thiele, G.; Woditsch, P. *Angew. Chem.* **1969**, *81*, 706; *Angew. Chem., Int. Ed. Engl.* **1969**, *8*, 672.
(34) Wiese, U.; Schäfer, H.; von Schnering, H. G.; Brendel, C.; Rinke, K. *Angew. Chem.* **1970**, *82*, 135; *Angew. Chem., Int. Ed. Engl.* **1970**, *9*, 158.
(35) Ziman, J. M. *Principles of the Theory of Solids*; University Press: Cambridge, England, 1964.
(36) (a) Hoffmann, R. *J. Chem. Phys.* **1963**, *39*, 1397. (b) Ammeter, J.; Bürgi, H.-B.; Thibeault, J. C.; Hoffmann, R. *J. Am. Chem. Soc.* **1978**, *100*, 3686. (c) Whangbo, M.-H.; Hoffmann, R.; Woodward, R. B. *Proc. R. Soc. London, A* **1979**, *366*, 23.

Table II. Madelung Factors for MX_3 Structural Models and Representative Ionic Energies (eV) for Trihalides[a]

case no.	structural arrangement	Madelung constant	structure type
	Hexagonally Close Packed Anions		
1	...B(α)C(α)...	5.132	TiI_3
2	...B(α)C(β)...	5.868	
3	...B(α)C(β)B(γ)C(α)B(β)C(γ)...	5.891	RhF_3
4	...B($\beta\gamma$)C( )...	5.448	
5	...B($\beta\gamma$)C( )B($\alpha\gamma$)C( )B($\alpha\beta$)C( )...	5.459	BiI_3
	Cubic Close Packed Anions		
6	...B(α)C(β)A(γ)...	5.676	
7	...B($\beta\gamma$)C( )A($\eta\iota$)B( )C($\delta\zeta$)A( )...	5.459	$AlCl_3$
	Double Hexagonally Close Packed Anions		
8	...B(α)C(α)B(ι)A(ι)...	5.412	

	ionic energy, eV		
halide	TiX_3	BiI_3	RhF_3
F	109.2 eV	116.2 eV	125.4 eV
Cl	89.4	95.1	102.6
Br	84.6	90.0	97.1
I	78.3	83.3	89.9

[a] Key: α, (0,0); β, ($^1/_3$, $^2/_3$); γ, ($^2/_3$, $^1/_3$); δ, ($^1/_3$, 0); ζ, ($^2/_3$, $^2/_3$); η, ($^2/_3$, 0); ι: ($^1/_3$, $^1/_3$).

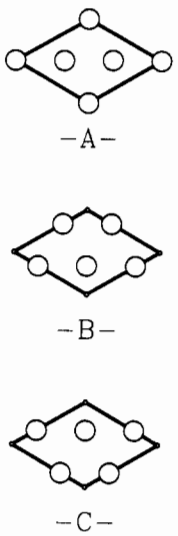

Figure 5. Scheme used in Table II to examine different structural topologies of MX_3 compounds.

The Ionic Model: The MF_3 Series

Since most of the structures involve a close packed arrangement of halides with metal atoms occupying one-third of the octahedral holes, we carried out Madelung calculations on model structures with idealized packing geometries, i.e., with regular octahedral and tetrahedral holes and equal metal–anion distances, and have summarized the results in Table II. The model structures are described by the positions of the anions (sheets A–C in Figure 5) in projection along [001]. When known, we report the structure type for a particular configuration.

Due to the large charge assigned to the metal ions, the arrangement of cations within the close-packed anion array that maximizes their mutual separation gives the lowest Madelung energy. This corresponds to the RhF_3 structure type, which offers the maximum M–X–M angle (132°) and a uniform distribution of occupied octahedral holes (one-third occupation of each close packed layer of possible metal sites). In general, the Madelung terms decrease as one proceeds from three-dimensional networks to two-dimensional layers and then to one-dimensional chains. Along this series, both the metal–metal distances and the M–X–M angle decrease. If we insert the average metal–halide distance into the expression for the Madelung part of the lattice energy, then we find the largest differences occur for the trifluorides—these

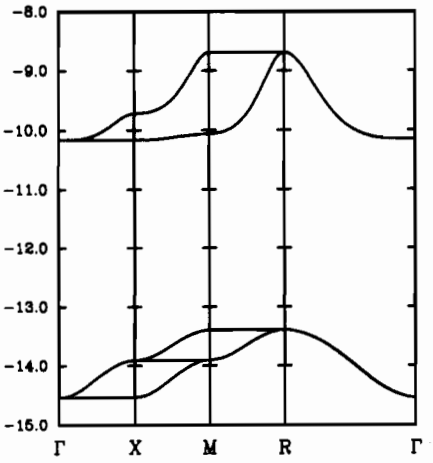

Figure 6. Dispersion of the 4d bands of RuF_3 in the cubic ReO_3 structure type. The bands centered around −14.0 eV are derived from the Ru t_{2g} orbitals and those around −9.0 eV are from the e_g orbitals. The labels correspond to high symmetry points in the first Brillouin zone: Γ = (0,0,0); X = ($^1/_2$,0,0); M = ($^1/_2$,$^1/_2$,0); R = ($^1/_2$,$^1/_2$,$^1/_2$).

compounds certainly have a large ionic component. How significant is the covalent part of the chemical bonding in these systems?

With respect to the RhF_3–VF_3–ReO_3 series, the cubic ReO_3-type always represents the minimum in ionic energy due to linear M–F–M angles. Therefore, M–F covalent forces must contribute significantly to the observed geometries for the MF_3 series. Figure 6 illustrates the band structure along various directions in reciprocal space for the d orbitals of RuF_3 in the ReO_3 structure type. The widths of the t_{2g} and e_g bands are relatively narrow (1.2 and 1.5 eV, respectively), and their extrema occur at the two points in the Brillouin zone that have $m\bar{3}m$ symmetry, Γ(0,0,0) and R($^1/_2$,$^1/_2$,$^1/_2$). Therefore, at these two points, the d bands rigorously transform as t_{2g} and e_g. Four representative orbitals are shown in **1**–**4**. Due to the imposed phase factors, the t_{2g}(Γ) orbitals have *no* ligand character, while those at R have maximum Mdπ–Fpπ antibonding overlap. The e_g orbitals, on the other hand, have ligand character throughout the Brillouin zone with Mdσ–Fsσ antibonding character at Γ and Mdσ–Fpσ antibonding character at R.

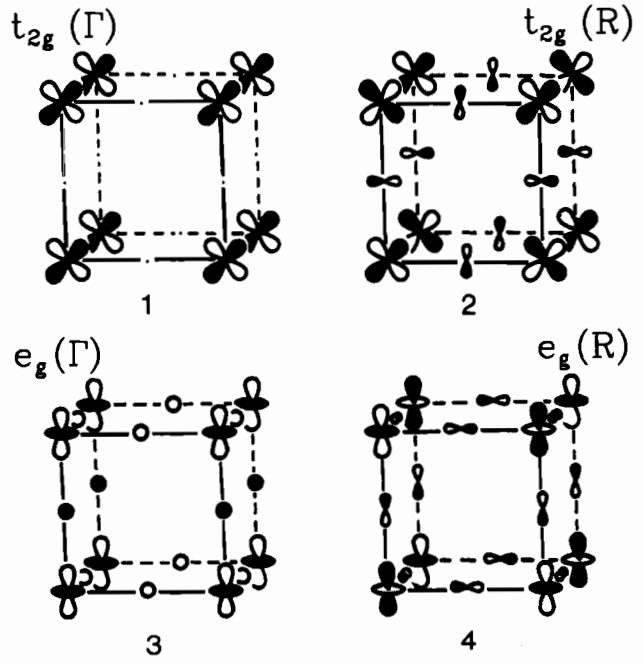

When the M–F–M angle is bent, both first- and second-order terms in the perturbation expansion of the orbital energies contribute to stabilization of the nonlinear geometry at certain electron counts. For the e_g band, bending reduces the Mdσ–Fs,pσ overlap to lower its average energy. Regardless of the direction of the bending mode at F, only one of the t_{2g} orbitals at R will become stabilized due to changes in overlap. Second-order mixing between the t_{2g}(R) level and the e_g(Γ) level can enhance the stabilization of the top of the t_{2g} band. For this effect to occur between two orbitals ψ_1 and ψ_2, in general, the matrix element $\langle\psi_1|\partial H|\partial q|\psi_2\rangle$ must be nonzero, i.e., transform as the a_{1g} irreducible representation, where the operator $\partial H/\partial q$ represents how the Hamiltonian changes under the distortion coordinate q.[37,38] Now, from Figure 6, we can choose $|\psi_1\rangle$ and $|\psi_2\rangle$ as the orbitals labeled t_{2g}(R) and e_g(Γ), respectively. The matrix element of the coupling will be nonzero when the direct product (t_{2g}(R) ⊗ χ($\partial H/\partial q$) ⊗ e_g(Γ)) contains a_{1g}(Γ). Therefore, the vibrational modes coupling these two orbitals must transform as either t_{1g}(R) or t_{2g}(R). The transformation from the ReO_3-type to the VF_3-type, as described by Michel[9] as well as Hyde and Andersson,[39] reduces the space group from $Pm\bar{3}m$ to $R\bar{3}c$ and corresponds to a t_{1g}(R) distortion coordinate. Application of the Landau theory[40] indicates that this transformation may be a second-order transition with both t_{1g}(R) and t_{2g}(R) irreducible representations accounting for the proper distortion coordinates.

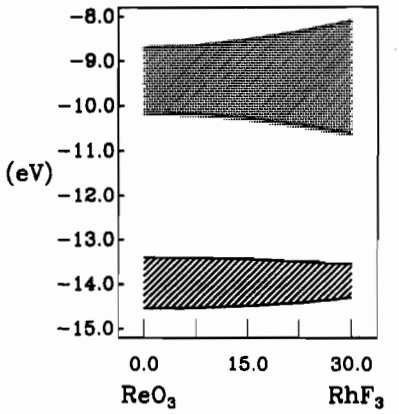

Figure 7. Variation in the dispersion of the t_{2g} and e_g bands vs angular distortion in the VF_3 series of trifluorides. The angle refers to the angle θ referenced in Hyde and Andersson[39] for BX_3 structures with $R\bar{3}c$ space groups and not the M–F–M angle in each system.

One final point concerns how the bottom of the t_{2g} band changes upon bending. The main perturbation is first order because decreasing the metal–metal separation will slightly increase the antibonding overlap within the t_{2g}(Γ) orbital between two metal sites. Thus, as a function of decreasing M–F–M angle, the t_{2g} bandwidth decreases, while its average energy remains unchanged. On the other hand, an enhanced antibonding interaction between metal sites at the top of the e_g band causes this band to have an increased bandwidth with a constant average band energy. Therefore, although the M–F distances decrease along the series from NbF_3 to RhF_3, which should lead to a stronger ligand field at the metal, the t_{2g}–e_g band splitting will remain nearly unchanged or slightly decrease. These conclusions are summarized in Figure 7.

We can now understand a large amount of structural data and physical measurements from this simple analysis. To conveniently summarize our conclusions, Figure 8 illustrates the differences in total electronic energy between the ReO_3-type and the RhF_3-type as the d electron configuration changes. Due to changes in F–F repulsions, the calculations of the two structures were carried out at different unit cell volumes so as to normalize the F–F interactions.

(37) Burdett, J. K. *Molecular Shapes*; Wiley: New York, 1980.
(38) Albright, T. A.; Burdett, J. K.; Whangbo, M.-H. *Orbital Interactions in Chemistry*; Wiley: New York, 1985.
(39) Hyde, B. G.; Andersson, S. *Inorganic Crystal Structures*; Wiley-Interscience: New York, 1989.
(40) Franzen, H. F. *Physical Chemistry of Inorganic Crystalline Solids*; Springer-Verlag: Berlin, 1986.

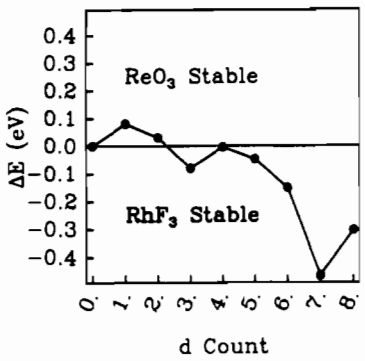

Figure 8. Energy difference curve between RhF_3 (hcp) and ReO_3 (defect ccp) structures for MF_3 as a function of the d electron configuration at the metal. Metal parameters were chosen for Ru.

Due to the small t_{2g} bandwidths, for d configurations less than d^3, the ReO_3-type is favored. At d^3, e.g., in MoF_3, the effects of first- and second-order mixing will lead to distortion toward the VF_3-type. We should point out that a slight amount of oxide impurity will reduce the electron configuration at the metal and stabilize the ReO_3-type as observed in the $Mo(O,F)_3$ system.[15] In addition, since we have adopted a semi-localized approach, the coupling of spins on adjacent d^3 metal centers should be antiferromagnetic through a superexchange mechanism via the bridging fluorides. Since the three t_{2g} orbitals are oriented in three mutually perpendicular planes, the orbitals are orthogonal to each other, and the overall magnetic moment per d^3 cation should show an $S = {}^3/_2$ effect at low temperatures, which agrees with the neutron diffraction data.[17]

For higher d electron configurations, we expect the VF_3 geometry to be preferred: least for d^4 and greatest for d^6. Although no technetium and rhenium trifluorides are known, RuF_3, RhF_3, and IrF_3 all adopt some variant of VF_3. While the d^6 systems are both diamagnetic, the magnetic properties of RuF_3 demand further investigation. With one unpaired electron per Ru center, we must consider at least two possible scenarios: (1) two dimensional antiferromagnetism, in which the same t_{2g} orbital at each metal site contains an unpaired electron; (2) one where each Ru atom is a paramagnetic center weakly coupled to (or even completely decoupled from) its neighbors. In case 1, the mechanism of spin coupling follows the MoF_3 example, while in case 2, the orthogonality of the three t_{2g} orbitals eliminates the superexchange mechanism. Spin–orbit splitting of the resulting $^2T_{2g}$ ground state could lead to a vanishing magnetic moment per Ru atom. The neutron diffraction results on RuF_3 report no antiferromagnetic ordering as well as no paramagnetic background, which would currently support case 2.[17] However, further studies need to be carried out in order to completely understand its magnetic properties.

Beyond d^6 systems, only the d^7 PdF_3 example has been reported. Original reports assigned the space group $R\bar{3}c$ to the crystal structure, and these calculations certainly confirm that when the e_g band is occupied, M–F–M will gain electronic energy by bending. A careful diffraction experiment, however, revealed that there were two inequivalent Pd ions in the structure, but both in a regular octahedral environment, which implies a formulation $Pd^{2+}Pd^{4+}F_6$.[11] Figure 9 shows the effect on the density of states (DOS) of the d bands as the VF_3-type transforms into the PdF_3-type. The e_g band splits into two narrower bands, and the formally d^7 system gains electronic energy. The two additional electrons assigned to the Pd^{2+} center, by Hund's rules, will form a local triplet, $^3A_{2u}$ ground state (as in NiO[41]). How these centers are coupled is shown via a simple molecular orbital diagram in Figure 10. Two Pd^{2+} ions are coupled via an intervening "$[Pd^{4+}(F^-)_2]$" complex. The results of the simple MO picture predict a ground state for this total complex with two unpaired spins: the Pd^{2+} ions are ferromagnetically coupled, which agrees with experimental observations. When the bridging complex is a d^{10} ion, like Sn^{4+}, then the coupling is weakly antiferromagnetic, or even zero.

(41) Goodenough, J. B. *Prog. Solid State Chem.* **1965**, *5*, 145.

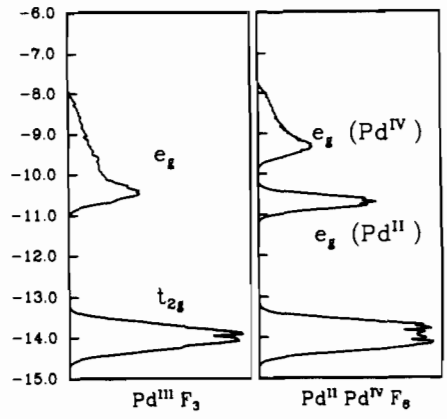

Figure 9. Energy density of states (DOS) for (left) PdF_3 in the undistorted ($R\bar{3}c$) RhF_3 structure and (right) PdF_3 in its observed ($R\bar{3}$) structure. Note that the e_g band splits into two separate energy bands. The narrow band at −10.5 eV in PdF_3 is half-occupied.

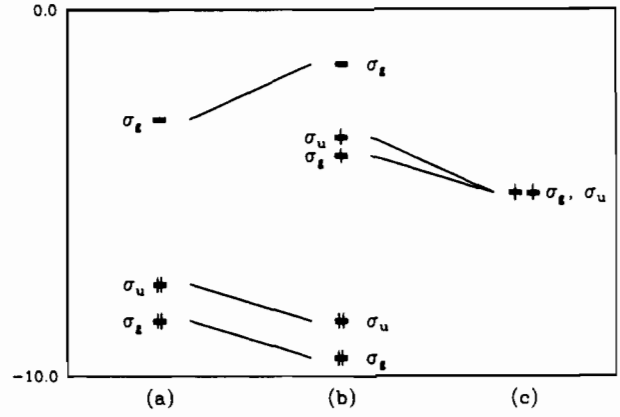

Figure 10. Interaction diagram between a model $[Pd^{4+}]F_2$ fragment (a) with two Pd^{2+} centers (c) to give a linear Pd–F–Pd–F–Pd fragment (b). Only the x^2-y^2 orbitals on the metal atoms are treated, and in octahedral coordination, each Pd^{2+} center has one electron in this orbital. The argument is similar for the z^2 orbitals. With six electrons and a small ΔE between σ_g and σ_u, a high spin or ferromagnetic ground state is favored.

We see that simple orbital-based arguments can account for numerous observations in the transition metal trifluorides. Although Madelung forces contribute primarily to the topology of their structures, M–F covalent forces strongly participate to influence the final structural details as well as to contribute to their magnetic phenomena.

Structural Variations in the Layered Trihalides

The structural preference within the series of trifluorides is dominated by the nature of the M–F covalent interaction. As we move to the heavier halides, i.e., as the anion polarizability increases, lower dimensional structures become prevalent. For these materials, three major interatomic interactions influence the observed geometries: (1) the ligand field effects of halide ions on the d orbitals of the transition metal; (2) through-space metal–metal interactions; (3) the matrix effect of halide ions. As the d configuration varies from d^0 to d^6 for a specific structure type and a given anionic matrix, the ligand field and metal–metal interactions will change, while the matrix effect remains essentially constant. In the $AlCl_3$ and BiI_3 structure types, the layers are held together by van der Waals interactions, which we can include into the matrix effect and presume constant for all of the compounds considered. Therefore, we shall concentrate on the interactions within each two-dimensional layer.

d^0 and d^6 Metals. We previously introduced the $AlCl_3$ structure as ccp anions with a honeycomb distribution of metal ions in the

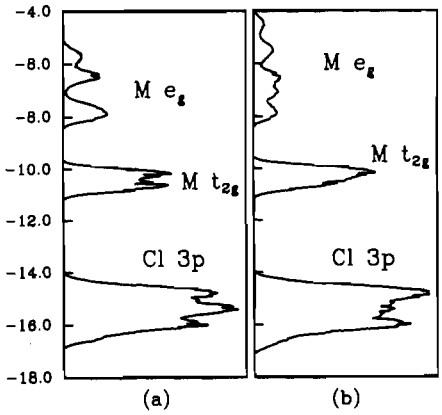

Figure 11. Total DOS curves for MCl_3 in (a) the undistorted $AlCl_3$-type and (b) the distorted $AlCl_3$. Distortions refer to positions of the halide anions; see text. Bands may be assigned as follows: (i) around −15.0 eV, Cl 3p (ii) around −10.3 eV, M t_{2g}; and (iii) around −6.5 eV, M e_g.

octahedral holes. However, in the observed structures of both d^0 and d^6 systems, the halides slip away from these idealized positions to increase the size of the octahedral sites left vacant within each occupied metal layer (see Figure 2a), although this occurs to a much greater extent in d^0 compounds. The metal atoms, herein, retain their regular honeycomb network during the anion distortion. The nature of the anion displacements are, of course, related to the crystal symmetry ($2/m$ in monoclinic $AlCl_3$, $\bar{3}m$ in rhombohedral BiI_3), but the magnitudes may differ from one compound to another.

The effect of these anion displacement on the total DOS is diagramed in Figure 11, which shows the Cl 3p and M 4d bands (the d orbitals are split into the characteristic "t_{2g}" and "e_g" sets of an octahedral ligand field). We can summarize the results as follows: (i) the Cl 3p band is slightly broadened by 0.50 eV with an increased DOS near the bottom of this band for the distorted variant; (ii) the M t_{2g} band becomes narrower by 0.25 eV with its average band energy increased; (iii) the M e_g band is pushed to higher energies by approximately 1.0 eV with a bandwidth increased by 0.5 eV. The changes in average band energy as the distortion proceeds simply reflect the increased ligand field imparted to the metal: M–Cl bonding orbitals are stabilized while the antibonding counterparts are destabilized. A more subtle conclusion arises from the changes of the t_{2g} band, whose narrowing occurs at the bottom via second-order mixing with orbitals near the top of Cl 3p levels. The anion distortion, therefore, will clearly benefit d^0 systems, but may have little or no effect on d^6 systems. Using coordinates from α-$RhCl_3$, we calculate an energy gain per formula unit of 2.24 eV for d^0 and −0.20 eV (destabilized) for d^6 systems. Indeed, YCl_3 and $LuCl_3$ show much larger deviations from idealized close packed arrangements than $RhCl_3$ or $IrCl_3$.[7] This result also informs us that the geometry of compounds with lower d-occupation in the t_{2g} bands will be more sensitive to the intensity of the ligand field than those with higher d counts.

d^1, d^3, and d^5 Metals. Since d^0 and d^6 metal ions have totally symmetric ground states in an octahedral field, distortions in their first coordination sphere are minimal when compared (usually) to those for intermediate d counts. In the d^3 molybdenum trichlorides, not only is there a slight distortion of the anion framework but also the honeycomb net of Mo atoms distorts to form Mo–Mo pairs. For α-$MoCl_3$, which adopts the monoclinic $AlCl_3$ structure, the displacement of Mo atoms is along the b axis, so that all of the symmetry of $AlCl_3$ structure type remains during the metal displacements. As for β-$MoCl_3$, the orientation and magnitude of the metal atom shifts are similar to α-$MoCl_3$; the space group differs due to a different stacking pattern of the individual layers. For the sake of our band structure calculations, the displacements of Mo atoms in both cases are identical, and we shall only focus on the distortion of the metal atoms in the two dimensional layer of α-$MoCl_3$ in the following discussion.

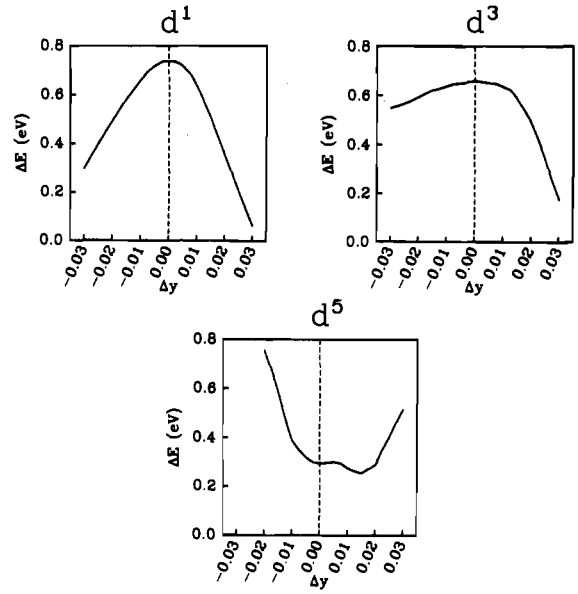

Figure 12. Variation in the total energy per formula unit for the $AlCl_3$ structure as a function of the metal–metal distance. These distances are represented as changes in the y parameter of the metal. $\Delta y > 0$ corresponds to the dimerization mode **5**, and $\Delta y < 0$ corresponds to the antidimerization mode **6**. The three curves are for d^1, d^3, and d^5 systems, respectively.

The symmetry of the undistorted layer, when it is removed from the complete $AlCl_3$ structure, is $\bar{3}m$ (D_{3d}).

The crystallographic sites of the metal atoms in $AlCl_3$ (space group $C2/m$) are $(0, y, 0)$ and $(0, \bar{y}, 0)$, and so we can examine the allowed displacements by changes in the y parameter. Since the metal atoms in the structure are related by the crystallographic 2-fold axis through the origin (and perpendicular to each layer), only two kinds of metal displacements are possible that retain the original space group: "dimerization" and "antidimerization," as shown in **5** and **6**. Clearly, **5** leads to distinguishable Mo_2 dimers

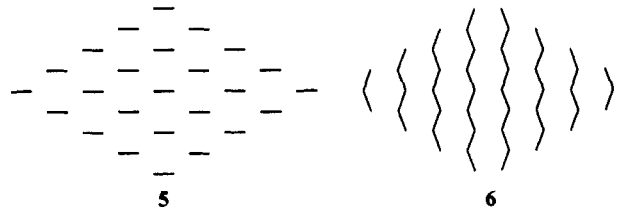

while **6** produces $^1_\infty[Mo_2]$ zigzag chains within the close-packed halide ions. Both distortion coordinates lead to $2/m$ (C_{2h}) symmetry for the MX_3 layer. Mode **5** has been reported not only for α-$MoCl_3$ and β-$MoCl_3$ but also for α-$TiCl_3$[42] and α-$RuCl_3$.[31] Mode **6** has yet to be conclusively observed, although previous theoretical investigations[42] on α-$TiCl_3$ suggested this to be the preferred distortion coordinate. We shall address this question later in this section.

Figure 12a–c illustrates the dependence of the total energies on small displacements of the metal atoms for d^1, d^3, and d^5 trichlorides. For the d^3 case, the regular hexagonal network of metal atoms represents a relative maximum in the total energy curve. Antidimerization provides just a slight decrease in total energy, while the dimerization mode shows a sharp energetic stabilization when the displacement goes beyond $\Delta y \sim 0.015$ (Mo–Mo distances $\sim$ 3.15 Å). For the d^1 configuration, both distorted variations are clearly favored over the $\bar{3}m$ (D_{3d}) layer, with dimerization as the slightly preferred configuration. The behavior of the low-spin d^5 system, however, is different. There are two energy minima. One of them, with a metal displacement of $\Delta y = -0.004$, corresponds to chain formation, while the other,

(42) Troyanov, S. I.; Snigireva, E. M.; Rybakov, V. B. *Russ. J. Inorg. Chem.* **1991**, *36*, 634.

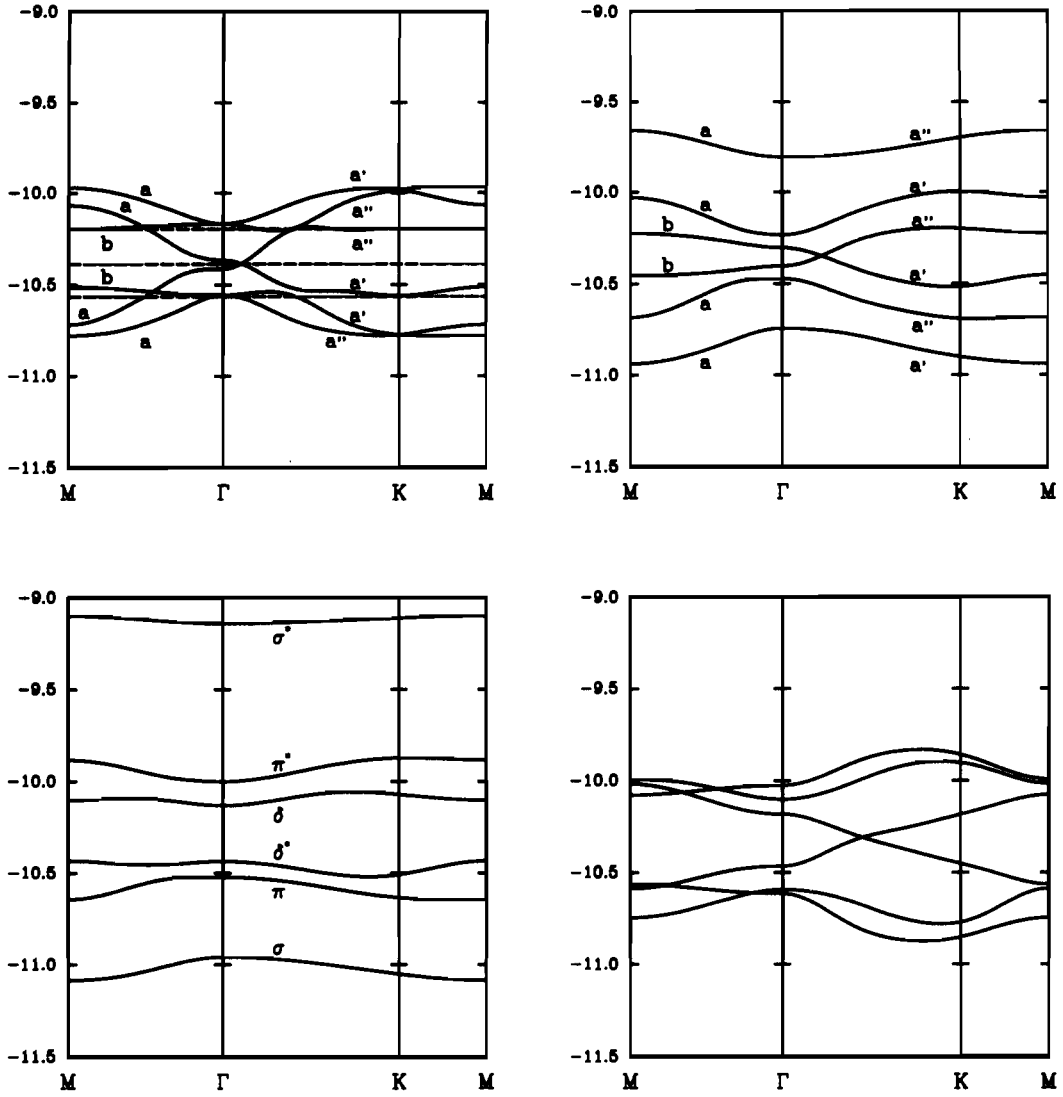

Figure 13. Energy band structure of the Mo t_{2g} orbitals along two directions in the Brillouin zone for $MoCl_3$ under different distortions: (upper left) trigonal system, all Mo–Mo distances are 3.46 Å, dashed lines are Fermi levels for d^2, d^3, and d^4, respectively; (upper right) dimer, short Mo–Mo distance is 3.16 Å; (lower left) dimer, short Mo–Mo distance is 2.80 Å, labels indicate type of metal–metal orbital interaction; (lower right) antidimer, long Mo–Mo distance is 3.76 Å.

with a displacement of $\Delta y = 0.015$, is a displacement toward dimers. In all of these three electronic configurations, therefore, the distortion toward dimerization (to varying extents) is more favorable than either the regular or antidimerization mode. For α-$MoCl_3$, the displacement of Mo atoms away from their regular positions has a large value of $\Delta y = 0.033$, while the shift in α-$TiCl_3$ is smaller. α-$RuCl_3$ is reported in the trigonal $P3_121$ space group, but recent scanning electron micrographs reveal a distortion of the chloride framework at the surface of the sample, which implies a slight dimerization of Ru atoms.[31] At this point, we should point out that the curves in Figure 12 arise for only metal displacements within an unmodified regular close packed array of halides. As Hyde and Andersson clearly state,[39] the halides will necessarily shift as the metal atom displacements occur. The increased repulsions between anions will affect these energy profiles mostly at Δy values far from 0.0. We investigate these matrix effects for α-$TiCl_3$ in a subsequent article.

For the second-row metals, experimental evidence, particularly magnetic susceptibility measurements, indicates low spin configurations. Therefore, in the analysis of the electronic structure, we need only consider occupation of the t_{2g} bands. Figure 13 shows how the band structure of a $MoCl_3$ sheet varies with Δy along two high symmetry directions in the Brillouin zone. The bands are labeled according to their irreducible representations or the character of the predominant metal–metal overlap. The line MΓ has a 2-fold rotation axis (parallel to a M–M bond), and the line ΓKM contains a mirror plane (perpendicular to a M–M bond). Only for the regular $AlCl_3$-type layer do Γ and K have the point symmetries $\bar{3}m$ (D_{3d}) and 32 (D_3), respectively. Upon distortion, the 3-fold rotation axis is lost, but the aforementioned 2-fold axis and mirror plane remain. Therefore, the most dramatic changes in the band structure occur near the Γ and K points. At Γ in the regular $AlCl_3$ net, the bands transform (increasing in energy) as $e_g + a_{1u} + a_{1g} + e_u$. The effect of M–Cl–M through bond coupling sets the M–M σ-bonding level slightly above the M–M σ-antibonding orbital (these levels are the two nondegenerate levels near −10.4 eV). Upon dimerization, the loss of the 3-fold axis at Γ causes the two doubly degenerate levels to split into the following representations: $e_g \rightarrow a_g + b_g$; $e_u \rightarrow a_u + b_u$. Increasing the extent of distortion shifts these energy levels until a gap for the d^3 configuration opens when the a′ and a″ bands finally cross. The band gap, then, continues to increase as the metal–metal distance becomes progressively shorter.

For α-$MoCl_3$, the significant feature of its band structure is that the t_{2g} bands are nearly independent of **k**, which indicates that the interactions between adjacent metal pairs is very weak, so that the Mo–Mo dimer in α-$MoCl_3$ and β-$MoCl_3$ may be considered as a nearly isolated molecular complex. The six d electrons of the $[Mo_2]^{6+}$ fragment completely occupy the three lowest t_{2g} bands, which should lead to diamagnetic and semiconducting behavior for these two systems. The observed magnetic susceptibility of α-$MoCl_3$, measured by Schäfer and von Schner-

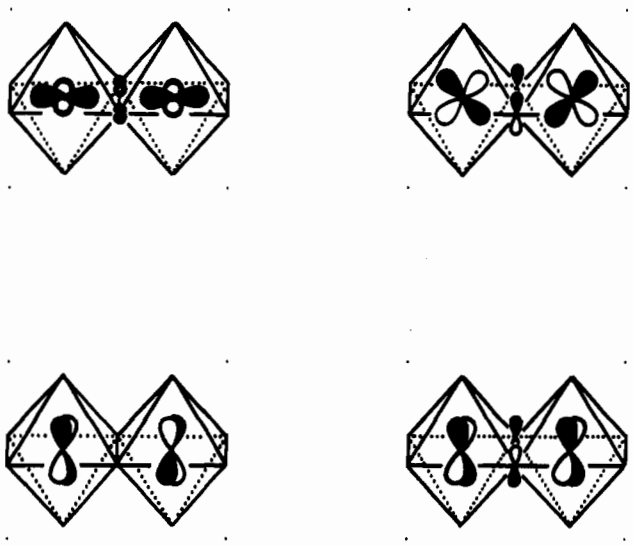

Figure 14. Orbitals (at the Γ point) near the Fermi level in $MoCl_3$. As discussed in the text, the three occupied orbitals have Mo–Mo σ, π, and δ^* character within the dimer, while the LUMO has Mo–Mo δ character.

ing, shows a rather complicated variation with the Cl/Mo ratio.[23] For Cl/Mo slightly less than 3.00, it is diamagnetic. When Cl/Mo is close to 3.00, it becomes temperature independent paramagnetic, and increasing the ratio beyond 3.00 leads to temperature dependent paramagnetism. But even for larger Cl/Mo ratios, the absolute values of the susceptibilities are still very small (μ_{eff} = 0.62 for Cl/Mo = 3.02 at room temperature). The composition dependence of the magnetic susceptibility is attributed to the incorporation of Mo ions with a higher oxidation state via Mo vacancies in the dimers.

Analysis of the chemical bonding in the α-$MoCl_3$ system suggests an alternative mechanism for the unexpected magnetic property of $MoCl_{3.00}$. In Figure 14 we diagram the three occupied t_{2g} orbitals plus the LUMO in $MoCl_3$ (these orbitals are drawn for the Γ point, but these characters remain throughout the Brillouin zone). Through-space overlap of the metal σ and π orbitals significantly stabilize these levels in the dimerized case, while through-bond coupling dominates in the δ orbitals. We can, therefore, conclude that the Mo–Mo bond order is slightly smaller than a typical double bond, due to the configuration $(\sigma)^2(\pi)^2(\delta^*)^2$. Since the HOMO and LUMO for α-$MoCl_3$ have δ^* and δ character, respectively, the ground state of this complex may acquire some triplet character due to configuration interaction, and show temperature independent paramagnetism via a second-order Zeeman effect.

Although we have examined in detail how the electronic structure and bonding are affected by metal dimerization for the d^3 system, we have not discussed the driving force for this particular distortion. The symmetrical nature of the band structure for the regular net (see Figure 13) and the position of the Fermi level for d^3 suggest that all metal–metal bonding levels are fully occupied in the metallic system. The variation of the metal–metal overlap population with d electron configuration confirms this point. Since this is exactly the half-filled band, we may hypothesize some kind of Peierls distortion to occur that breaks the "accidental" degeneracy along the ΓKM line. However, the dimerization mode is a *translationsgleich* operation (i.e., the size of the unit cell is preserved), and it does not remove the degeneracy. Furthermore, the shape of the total energy curve as Δy varies (see Figure 12) is clearly anharmonic near $\Delta y = 0$. Therefore, the existence of Mo_2 dimers is clearly important as the two-dimensional structure grows, and we do not expect a phase transition to the more symmetrical geometry at higher temperatures. Even with one extremely short Mo–Mo distance in the two dimensional layer, the total M–M overlap population shows a strongly nonlinear, increasing variation with Δy (Figure 15).

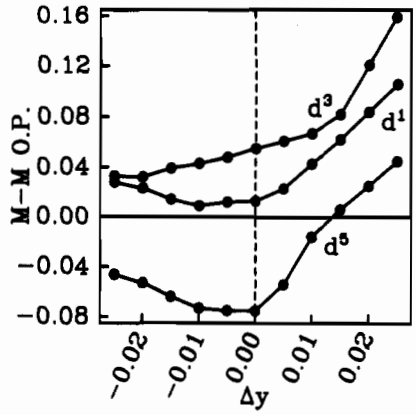

Figure 15. Variation in the total M–M overlap population as a function of Δy for the $AlCl_3/MoCl_3$ structural family. Only d^1, d^3, and d^5 systems are shown. With three nearest neighbor metals, the value of the overlap population is the sum of these three values. See text for further discussion.

Therefore, at d^3 counts, the formation of dimers is favored for all temperatures.

The preference for dimerization over antidimerization is also evident from Figure 15, in which we find low positive values for the total overlap population between d^3 metal centers. In fact, for the three systems d^1, d^3, and d^5, the formation of one short and two long metal–metal distances (**5**) in the hexagonal network of $AlCl_3$-type solids provides greater total bonding character between metals than one long and two short distances (**6**). For d^5 metals, the total metal–metal overlap population is net antibonding for a large range in Δy, but the network is less antibonding under mode **5** than under mode **6**. In fact, when Δy approaches 0.012, the interaction between metal centers becomes attractive, which indicates a significant bonding interaction within the dimer relative to between them.

As we mentioned previously, d^1 and d^5 trichlorides also exhibit metal–metal dimers in their structures. For the d^1 system, only α-$TiCl_3$ shows this type of layer structure, while Zr and Hf systems adopt a distorted TiI_3 structure. α-$RuCl_3$ (d^5) shows a distortion of the Ru network.[31] The total energy curve in Figure 12 suggests the dimerized structure to be just slightly favored, while the population curve in Figure 15 implies a stronger preference for the dimer. A recent X-ray diffraction study does indeed find the predicted mode.[43] The band structure diagrams (Figure 13) show that, as the dimers form, a small gap opens between the bottom five bands and the top σ^* band, due in large part to second-order mixing with the e_g levels.

The magnetic properties of α-$RuCl_3$ resemble those of the 3d systems $CrCl_3$ and $FeCl_3$, which are ferromagnetic within the two-dimensional layer and antiferromagnetic between layers.[29] This conclusion arises from a positive Curie temperature by extrapolating the high temperature susceptibility, and the Néel temperature near 15 K. From our band structure calculations, the band at the top of the t_{2g} manifold (labeled a″ along the ΓKM lines in Figure 13) splits away from the rest with an energy gap near 0.2 eV. We hypothesize that the spin-pairing energy within the Ru_2 dimers exceeds this gap and leads to two unpaired spins occupying an $a_g(\Gamma)$ and an $a_u(\Gamma)$ orbital for a ^3A_u ground state—a paramagnetic semiconductor. Optical spectra have been measured for this compound[44] and nicely confirm our band picture. The original classification of the optical transitions assumed that the Ru atoms are completely noninteracting in a trigonally distorted octahedral crystal field. However, the nature of the crystal field is significantly affected due to condensation of coordination polyhedra, and we propose the assignment in Table III from our band calculations. Although we have not illustrated the effects on the e_g bands in this contribution,[42] on account of

(43) Hönle, W. Private communication.
(44) Binotto, L.; Pollini, I.; Spinolo, G. *Phys. Stat. Sol.* **1971**, *B44*, 245.

Table III. Assignment of Optical Transitions in the Absorption Spectrum of α-$RuCl_3$

ΔE, eV	former assignment[44]	current assignment[42]
0.28	$^2T_2 \rightarrow {}^6A_1$	$^3A_u \rightarrow {}^3A_g$: $\delta^* \rightarrow \delta$
0.53	$^2T_2 \rightarrow {}^4A_1$	$^3A_u \rightarrow {}^3B_g$: $\pi^* \rightarrow \sigma^*$
0.75	$^2T_2 \rightarrow {}^4T_2$	
1.15		$^3A_u \rightarrow {}^3A_g$: $\sigma \rightarrow \sigma^*$
2.08	$^2T_2 \rightarrow {}^2T_1$	$^3A_u \rightarrow {}^3B_g$: $t_{2g} \rightarrow e_g$
2.33	$^2T_2 \rightarrow {}^2A_1$	$^3Au \rightarrow {}^3A_g$: $t_{2g} \rightarrow e_g$
2.66	$^2T_2 \rightarrow {}^2A_1$	$^3A_u \rightarrow {}^3B_g, {}^3A_g$: $t_{2g} \rightarrow e_g$
3.30	charge transfer	charge transfer
5.10	charge transfer	charge transfer
7.20	charge transfer	charge transfer

the edge-sharing octahedra, we find that this band is split into two sharp peaks, whose splitting is further enhanced upon distortion.

d^2 Metals. As Figure 13 illustrates, the d^2 and d^4 systems have Fermi levels that lie on "superdegenerate" bands, i.e., energy bands that show zero or nearly zero dispersion throughout reciprocal space.[45] This situation is reminiscent of the orbital degeneracy required for a first-order Jahn–Teller instability.[37] In an earlier investigation on rare earth hydride halides, systems can remove this degeneracy by either distortion or accepting interstitial species.[46] In the Nb and Ta compounds, we have a third solution: formation of a solid solution of metal triangles and dimers.[7] Careful analysis has revealed that "$NbCl_3$" is one component along a phase width between $NbCl_{2.67}$ and $NbCl_{3.13}$. At $NbCl_3$, we have a 2:1 Nb_3Cl_8:Nb_2Cl_8 ratio. In fact, for the general system, $NbCl_{3+x}$ under this two component model, the ratio of triangles to dimers is $(2-2x)/(1=3x)$. Therefore, near the maximum observed $x \sim 0.2$, this ratio is approaches 1. $TaCl_3$ shows a X-ray powder diffraction pattern similar to $NbCl_3$,[47] but McCarley and co-workers have demonstrated that $TaBr_3$ is a metastable phase that probably contains $[Ta_6Br_{12}]$ cluster units,[48] although there is no conclusive structural evidence as yet.

Figure 16 shows the total electronic energy for disproportionation of MX_3 into M_3X_8 and MX_4 for several cases: (i) three regular close packed halide nets with the metal atoms in the ideal octahedral holes, i.e., no strong metal–metal bonding component; (ii) a regular MX_3 net vs the M_3X_8 and MX_4 systems distorted to give triangular and dimeric clusters; (iii) an MX_3 layer distorted toward M–M dimers vs the M_3X_8/MX_4 system in case ii. The maximum driving force for disproportionation occurs at d^2 in the trihalide. Rather than adopt a $\sigma^2\delta^{*2}$ configuration with a net bond order slightly less than one, Nb and presumably Ta halides form triangular clusters with three M–M σ bonds and some excess dimers with the reduced bond order. Figure 17 compares the total DOS for Nb_3Cl_8 and $NbCl_4$. When both metal clusters occur together in a solid solution, they will adjust electron density to achieve the same chemical potential (Fermi level). Therefore, we expect charge transfer from the triangle to the dimer. At $NbCl_3$, oxidizing the Nb_3 triangles by one electron produces an electronically stable six-electron cluster and a Nb_2 dimer composed of d^2 metals, which is isoelectronic to the Mo dimers in $MoCl_4$.[49] For $-1/3 \leq x < 0$, only some of the triangles would be oxidized. At $x = 0$, the Fermi level is set by the dimers ($[Nb_2Cl_8]^{2-}$), as there is a gap between the three lowest levels in the triangle and the next highest orbital. As x increases above 0, the Fermi level will drop monotonically as the dimer units become oxidized, and the stability of this homogeneity range remains until E_F drops below the HOMO for the six-electron triangular cluster. At that point, the system then disproportionates into $NbCl_4$ and $Nb_{3-x}Cl_8$.

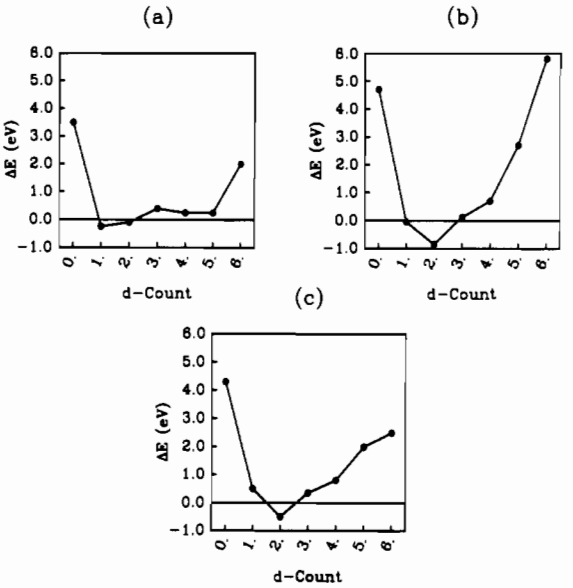

Figure 16. Electronic energy contribution to the disproportionation of MX_3 into M_3X_8 and MX_4 for three different cases. In each case, the halide ions form a close-packed arrangement. Key: (a) all metal atoms occupy the center of the octahedral holes (no M–M bonding); (b) M atoms shifted in M_3X_8 and MX_4 to form trimers and dimers, respectively; (c) M atoms shifted in all three systems to form trimers and dimers. $\Delta E > 0$, MX_3 preferred; $\Delta E < 0$, $M_3X_8 + MX_4$ preferred.

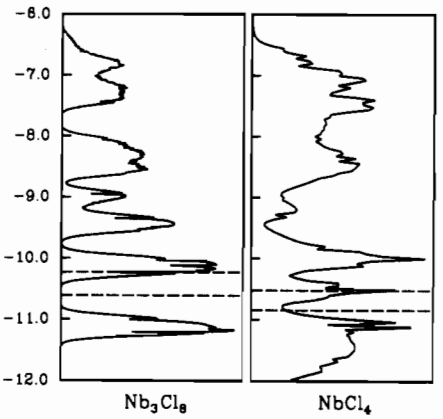

Figure 17. Total DOS curves for Nb_3Cl_8 and $NbCl_4$. Fermi levels are for 70 and 71 valence electrons in Nb_3Cl_8 (6 and 7 cluster electrons), and 25 and 26 electrons in $NbCl_4$ (1 and 2 cluster electrons).

d^4 Metals. ReX_3 moieties all show variation from the $AlCl_3$-type layer. In fact, the metal ions are only five-coordinate to halide, with the vacant anion site now available to promote the formation of strong Re–Re bonds. Since metal–metal bonds occur for a variety of d counts, why does the ligand field in this series deviate from six-coordinate octahedral? We examine this question using the idea of pair potentials developed by Burdett and Fässler.[50] For octahedral complexes ML_6, pair potentials are evaluated by the expression

$$P = E(ML_6) + E(ML_4) - 2E(ML_5)$$

Since there are two possible geometries for the ML_4 fragment (square planar or sawhorse), we choose $E(ML_4)$ as the weighted average of these two configurations, in which the weighing factors are the fractions of possible square planar and sawhorse geometries. Figure 18 shows the pair potential for $[MCl_6]^{n-}$ between d^0 and d^6 electronic configurations. Although the potentials are all slightly repulsive, the largest values occurs between d^3 and d^4. This feature occurs because the loss of one π-donor ligand stabilizes two of the three t_{2g} (Re–Cl π^*) orbitals to give the greatest pair potential at the low-spin d^4 configuration.

(45) Hughbanks, T.; Kertesz, M. *Mol. Cryst. Liq. Cryst.* **1989**, *176*, 115.
(46) Burdett, J. K.; Miller, G. J. *J. Am. Chem. Soc.* **1987**, *109*, 4092.
(47) Schäfer, H.; Scholz, H.; Gerken, R. *Z. Anorg. Allg. Chem.* **1964**, *331*, 154.
(48) Converse, J. G.; Hamilton, J. B.; McCarley, R. E. *Inorg. Chem.* **1970**, *9*, 1366.
(49) Pisarev, E. A.; Drobot, D. V.; Makarchuk, I. V. *Russ. J. Inorg. Chem.* **1982**, *27*, 10.
(50) Burdett, J. K.; Fässler, T. F. *Inorg. Chem.* **1990**, *29*, 4594.

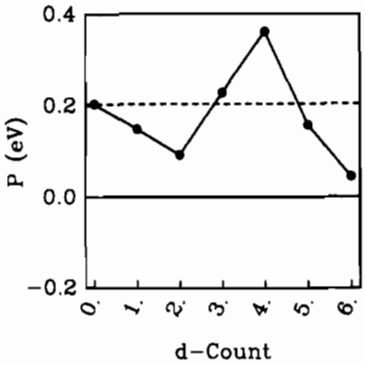

Figure 18. Value of the pair potential, P, for an $[MX_6]^{n-}$ octahedral complex as a function of d electron configuration. The dashed line equals P for the d^0 case. When P is above this line, the complex is more susceptible to loss of a halide ligand.

Reexamination of the WCl_3 structure shows 12 Cl–Cl separations of 2.23 Å per formula unit.[25] If we assume these to be $(Cl_2)^-$, then WCl_3 may be expressed as $W_6Cl^i_6(Cl^i-Cl^a)_6$ with W^{2+} ions (d^4). However, whether W is considered as d^3 or d^4 in this compound, the number of cluster valence electrons per W_6Cl_{12} cluster would range between 18 and 24; a value that is unusually high for this motif. We are currently pursuing how relativistic effects may perturb the distribution of cluster orbitals in these systems.[51]

For the ReX_3 series, two triangular motifs are possible, **7** and **8**, both of which have D_{3h} point symmetry. Case **7** is the one

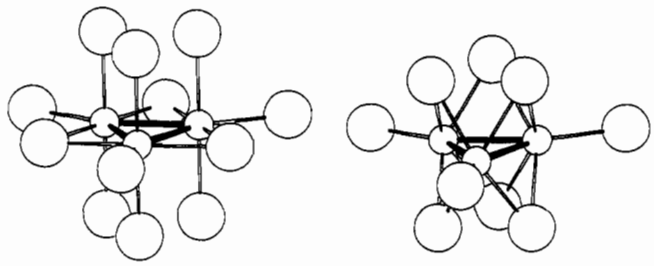

7 **8**

found in all ReX_3 phases, and consists of a Re_3 triangle whose edges are bridged by three coplanar halide ions. In fact, **7** represents $[Re_3Cl_{12}]^{3-}$ with the terminal halides shared between two adjacent clusters in ReX_9. In case **8**, the edges of the metal cluster are each bridged by two halides. The proper stoichiometry is achieved in this molecular entity, and no condensation is required. The inner cluster is observed, for example, in the $[Nb_3Cl_6(hmb)_3]^+$ cation.[52] The stability of **7** over **8** for d^4 metals may be rationalized by their molecular orbital energy diagrams in Figure 19. The stable electron counts for **7** and **8** are 12 and 8 (or possibly 10), respectively. Therefore, cluster **7** is a more electron rich system.

To understand the differences in chemical bonding between the two cluster motifs, we point out that the two moieties have a mirror plane that contains the three metal atoms. Orbitals symmetric with respect to this operation are labeled with a prime (a_1'), and those antisymmetric are labeled with a double prime (a_2''). In **7**, the six occupied orbitals in ReX_3 may be assigned to three σ-type bonds ($a_1' + e'$) and three π-type bonds ($a_2'' + e''$), or formally three Re–Re double bonds. On the other hand, in **8**, the most stable metal-centered orbitals may be assigned to three two-center two-electron σ bonds ($a_1' + e'$) plus one three-center two-electron "σ" bond and one three-center two-electron "π" bond. The bonding and electronic structure of these clusters have been carefully examined, and we refer the reader to some of the literature.[53]

Quasi-Infinite Chains

As Table I points out, all the heavier trihalides, i.e., the bromides and iodides, with d^1, d^3, d^5, and even d^2 transition metals adopt a variation of the TiI_3-type structure. For the chlorides, however, these structures occur only for the d^1 and d^5 transition metals. Obviously, the heavier halides prefer the chain-like structure, and the chlorides, the layered one. The reason for this structural preference is very similar to that of the geometrical variation in H_2Y molecules (Y = O, S, Se, Te), and may be understood by a fragment analysis. For both $AlCl_3$ and TiI_3 structure types, the anions are directly bonded to two metal atoms. Due to edge-sharing, the angle at the halide in the $AlCl_3$-type is near 90°, while in the face-sharing arrangement in the TiI_3-type, this angle is approximately 70.5°. (Note: ionic forces will tend to make these angles larger because the greater repulsion occurs between adjacent cations.[39]) Figure 20 illustrates the variation in energy of the 8-electron fragments, M_2F, M_2Cl, and M_2I (the metal atoms were modeled with Mo parameters), as the M–X–M angle changes. Clearly, the bending potential is highest for fluoride and lowest for iodide. These curves reflect the superposition of several effects, of which two important aspects are the matrix effect (occurring through the M–X distances) and the amount of sp hybridization (primarily controlled by the orbital exponents in the Slater functions). Of course, the polarizability of these anions increases from F to I,[54] and this factor rationalizes much of the structural chemical differences between fluorine and the rest of the halogens.[5] Therefore, bromide and iodide occur with the smallest M–X–M angles in the trihalide series. Nevertheless, the $AlCl_3$ layer structure is still more favorable than the TiI_3 chain at d^0 and d^6, even for the iodides. However, when metal–metal bonding takes effect (as we shall analyze shortly), the energetic preference for the layered compounds is lost for the bromides and iodides, but retained by the chlorides, except when this metal–metal interaction is significant.

Distortion of the TiI_3 Structure. The crystallographic studies on compounds with the TiI_3 structure have been historically slightly confusing. Early investigations assigned a hexagonal space group with equal M–M distances along the chain. However, extra X-ray reflections were often observed in some of the heavier trihalides, even for TiI_3 itself. Subsequent single crystal studies on, for example, $MoBr_3$,[24] $RuBr_3$,[30] and ZrI_3[19] revealed that these compounds actually crystallize in the orthorhombic space group, *Pmmm*, with two chains per unit cell. Two sets of atomic displacements occur from the idealized hexagonal setting to the orthorhombic cell: (i) the metal atoms slip away from their regular positions along the *c* axis to form M–M pairs; and (ii) the anions shift to form two different isosceles triangles bridging pairs of metal atoms; those shared between the short distance are larger than triangles between the long distance. In the complete three-dimensional structure, the alternation of M–M distances occurs in an "out-of-phase" fashion between the two chains in the unit cell. This "out-of-phase" displacement of the metal atoms forces the whole system to deviate from hexagonal and toward orthorhombic symmetry.

Metal–Metal vs Metal–Halide Bonding. These quasi-one-dimensional chain structures have already been extensively examined using extended Hückel calculations.[21] Therefore, we shall not dwell on all details of the band structure, but we shall comment on aspects pertinent to our argument. Since the primary interactions occur between metal and halide, the bands show a

(51) Miller, G. J. Unpublished research.
(52) King, R. B.; Braitsch, D. M.; Kapoor, P. N. *J. Am. Chem. Soc.* **1975**, *97*, 60.
(53) (a) Müller, A.; Jostes, R.; Cotton, F. A. *Angew. Chem.* **1980**, *92*, 921; *Angew. Chem., Int. Ed. Engl.* **1980**, *19*, 875. (b) Bursten, B. F.; Cotton, F. A.; Hall, M. B.; Najjar, R. C. *Inorg. Chem.* **1982**, *21*, 302.
(54) Pauling, L. *The Nature of the Chemical Bond*, 3rd ed.; Cornell University Press: Ithaca, NY, 1960.

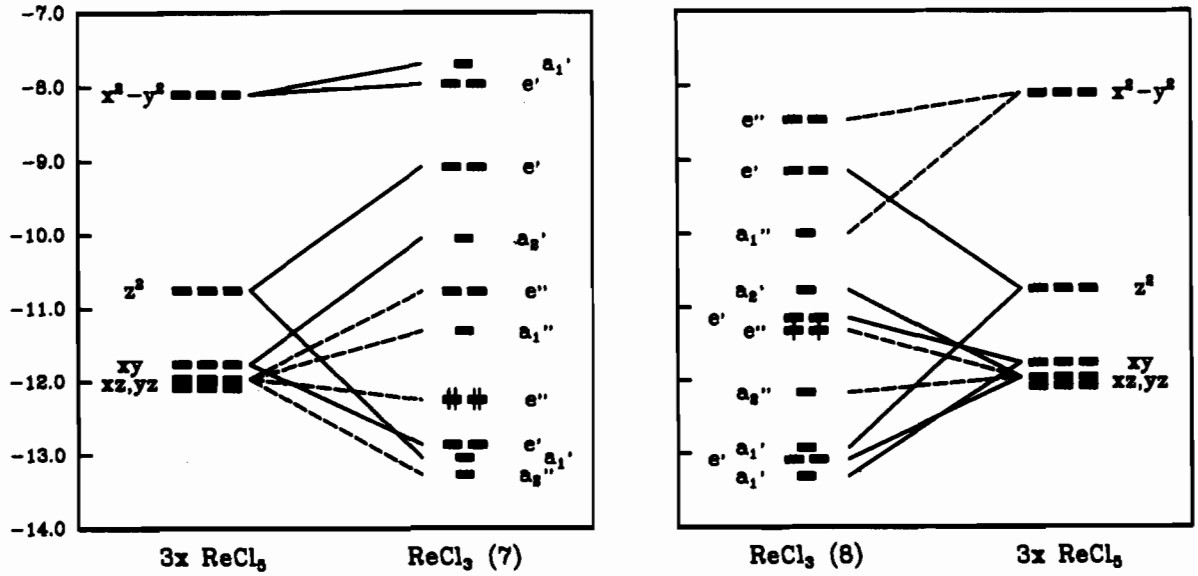

Figure 19. Correlation of the d orbital energies as three square pyramidal [$ReCl_5$] fragments are condensed to form the Re_3X_n clusters in **7** and **8**. The HOMO's for a Re^{3+} ion are respectively marked.

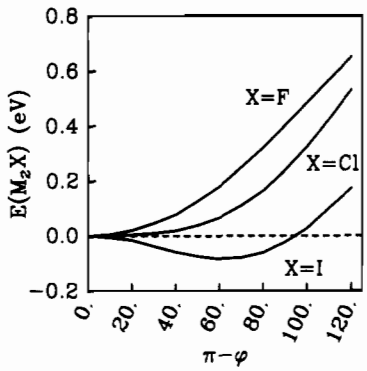

Figure 20. Energy of M_2X (X = F, Cl, and I) fragments vs M–X–M angle (ϕ). Only M–X orbital overlap is included in the calculation of these energy values.

typical octahedral splitting pattern with band dispersion arising from both metal–metal and metal–halide overlap between unit cells. In the t_{2g} band (we choose the z axis as the chain axis), the large σ overlap between z^2 orbitals on adjacent metals leads to a bandwidth of nearly 3.5 eV. The other t_{2g} orbitals show almost negligible dispersion, and have been labeled "localized".[21] Dispersion of energy bands, especially in transition metal systems, is controlled by two effects: (1) through-space overlap of orbitals on the metals; (2) through-bond coupling via bridging ligands. The second point has been examined by Hoffmann and Summerville for $[M_2X_9]^{3-}$ fragments.[55] In Figure 21, we compare the band structures along ΓZ for the cases when the through-space metal–metal overlap has been either turned off or on. The effect of through-bond coupling is significant for, when no metal–metal overlap is considered, the lowest bands have mostly metal–metal antibonding character. Also, the (δ,π) and (δ^*,π^*) bands show nearly 1.5 eV dispersion. When the metal–metal orbital overlap is included, the (σ,σ^*) band widens considerably and the π and δ overlap nearly negates the through-bond coupling effects to give two sets of nearly degenerate, dispersionless bands. At the zone edge, through-bond terms remain but the through-space terms in the equidistant chain are eliminated due to the imposed phase factors—through-space interactions along the chain become nonbonding. Therefore, the dispersionless π and δ bands in ZrI_3 are actually the result of two competing forces which make the bands energetically narrow. Although, the relative effect of onsite electron–electron repulsion will certainly be more influential in these orbitals, occupation of these bands play an important role in the structural observations for this series of compounds.

(55) Summerville, R. H.; Hoffmann, R. *J. Am. Chem. Soc.* **1979**, *101*, 3821.

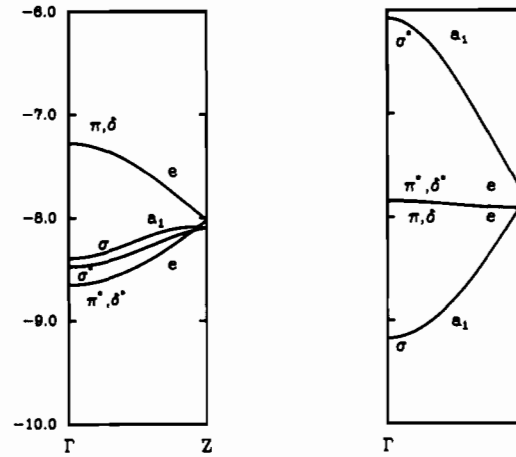

Figure 21. Band structures along ΓZ (Z = $c^*/2$) for a single $^1_\infty[ZrI_{6/2}]$ chain of confacial octahedra: (left) only Zr–I orbital overlap included; (right) Zr–I and Zr–Zr orbital overlap included.

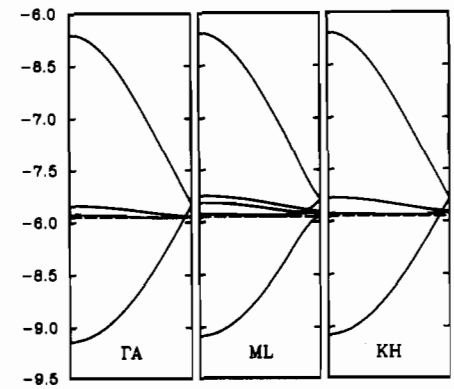

Figure 22. Band structures along ΓA, ML, and KH for the complete idealized hexagonal structure of "ZrI_3." (Γ = 0, 0, 0; A = 0, 0, $^1/_2$; M = $^1/_2$, 0, 0; L = $^1/_2$, 0, $^1/_2$; K = $^1/_3$, $^1/_3$, 0; H = $^1/_3$, $^1/_3$, $^1/_2$). The dashed line is the Fermi level for a d^1 system.

The Band Structure of the TiI_3 Structure. Figure 22 illustrates the band structure of the t_{2g} bands for the hexagonal TiI_3 structure (space group $P6_3/mmc$) along three high-symmetry directions. The screw axis accounts for the degeneracies at the $c^*/2$ plane. Since previous treatments of the bonding and electronic structure of these compounds have assumed isolated chains, i.e., they have

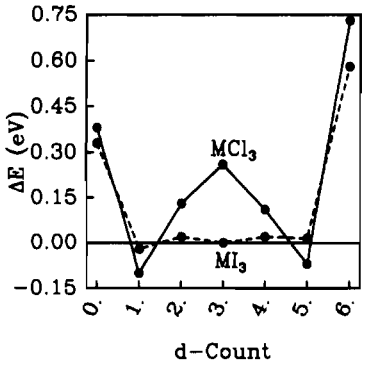

Figure 23. Energy difference curves between the $AlCl_3$ and TiI_3 structure types for both MCl_3 and MI_3 as a function of the d electron configuration at the metal. $\Delta E > 0$, $AlCl_3$-type preferred; $\Delta E < 0$, TiI_3-type preferred.

only examined the ΓA lines, the important differences in the band dispersion along the three parallel high symmetry lines in the three-dimensional Brillouin zone have been overlooked. The features of the bands along ΓA and KH are similar due to the 3-fold rotation axis. The different positions of the e bands reflect interchain orbital overlap, which primarily involves iodide orbitals. In both cases, the e bands converge to a lower energy than the z^2 bands at the zone edges due to second-order mixing with the e_g-type bands at higher energies. Of particular importance to this system, however, is the band structure along ML. The only symmetry operation that is retained along ML is a vertical mirror plane—the bands may be classified only as symmetric or antisymmetric with respect to this reflection. The consequence is an avoided crossing between the z^2-σ band and a symmetric component of the (π,δ) band. The Fermi level for d^1 systems touches the lowest degenerate pair at L, which contains a significant z^2 contribution. Therefore, the dimerization of metal atoms along the chains can be attributed to a Peierls distortion, and the transformation to an orthorhombic crystal system arises from this degeneracy at the L point ($^1/_2$, 0, $^1/_2$).

Chains vs Layers

As we have previously mentioned, the decision of a system to choose the layered $AlCl_3$-type or the one-dimensional TiI_3-type rests significantly on the halide and its relative polarizability. Smaller angles are preferred for the heavier halides, and the line of demarcation occurs between Cl and Br. At this level of semiempirical theory, we have not incorporated terms in the Hamiltonian related to these factors. However, the significant differences occur at the d^3 case, which implies a significant contribution from metal–metal interactions: both through-space as well as through-bond.

In Figure 23, we illustrate energy difference curves for both chloride and iodide systems between the two structure types as a function of d count. The energy differences consider only those terms associated with metal–metal interactions; i.e., energy differences arising from the different M–X–M angles and packing effects have been removed. The figure clearly shows the difference between MCl_3 and MI_3. Strong M–M σ bonding between z^2 orbitals leads to considerable preference for the TiI_3-type at d^1. Between d^2 and d^4, through-bond coupling is energetically important for the chlorides, which favors the layered structure. For the iodide, through-space and through-bond forces between metal atoms are comparable, and so we observe near zero energy differences. At d^5, all metal–metal σ, π, and δ bonding orbitals are occupied, as well as π^* and δ^*, so a situation similar to that at the d^1 count arises.

Table IV. Atomic Parameters Used in the Extended Hückel Calculations

atom	orbital	H_{ii}, eV	ζ_1	C_1	ζ_2	C_2
F	2s	−40.00	2.43			
	2p	−18.10	2.43			
Cl	3s	−26.30	2.18			
	3p	−14.20	1.73			
I	5s	−18.00	2.68			
	5p	−12.70	2.32			
Zr	5s	−9.87	1.82			
	5p	−6.76	1.78			
	4d	−11.18	3.84	0.6210	1.51	0.5769
Nb	5s	−10.10	1.89			
	5p	−6.86	1.85			
	4d	−12.10	4.08	0.6401	1.64	0.5516
Mo	5s	−8.77	1.96			
	5p	−5.60	1.90			
	4d	−11.06	4.54	0.5899	1.90	0.5899
Ru	5s	−10.40	2.08			
	5p	−6.87	2.04			
	4d	−14.90	5.38	0.5340	2.30	0.6365
Pd	5s	−8.64	2.19			
	5p	−2.68	2.15			
	4d	−12.65	5.98	0.5535	2.61	0.6701

Summary

This lengthy excursion into the electronic structure and bonding of the trihalides of the second- and third-row transition metals has once again stressed the importance of anion coordination in controlling solid-state structures. Although metal–metal bonding exerts structural influences and certainly contributes to physical and chemical properties, bonding occurs principally with and through the anions, and their chemical bonding requirements dictate the general structural topology. Therefore, we can find diverse dimensionality in this class of compounds which ranges from molecular species to three-dimensional networks. Ligand field effects are also important as witnessed in the d^4 systems of ReX_3. Five-coordination of the metal enhances metal–metal bonding toward the formation of high-nuclearity clusters.

Although our method has involved semiempirical methods, it has provided numerous interpretations in accord with experiment. We have presented a new assignment of the optical absorption spectrum of α-$RuCl_3$ that differs from earlier spectral assignments that did not take into account the effects of through-bond interactions on the ligand field at the metal ions—an important aspect in the structure and bonding of these trihalides.

Acknowledgment. The authors wish to thank Profs. J. D. Corbett, H. F. Franzen, and R. E. McCarley for helpful suggestions and discussions. This research was supported by an ISU University Research Grant.

Appendix

Most of the calculations described in this paper used the extended Hückel method within the framework of the tight-binding approximation.[36] The atomic parameters are listed in Table IV. Integrated quantities, e.g., total energies, charges, and overlap populations, as well as DOS diagrams, were determined by using special point sets[56] in the corresponding Brillouin zones. Madelung energies were calculated by using the Ewald method[35] and excluded all Born repulsion terms.

Experimentally determined metal–halide bond distances were used. When idealized coordination polyhedra were formed in our structural models, then the average metal–halide distance was included.

(56) Chadi, D. J.; Cohen, M. L. *Phys. Rev. B* **1973**, *8*, 5747.